Detection of nanobubbles on lubricant-infused surfaces using AFM meniscus force measurements

Sam Peppou-Chapman,[†,‡] Christopher Vega-Sánchez,[†,‡,¶] and Chiara Neto[*,†,‡]

†*School of Chemistry, The University of Sydney, NSW 2006 Australia*

‡*University of Sydney Nano Institute, The University of Sydney, NSW 2006 Australia*

¶*School of Electromechanical Engineering, Costa Rica Institute of Technology, 159-7050 Costa Rica*

E-mail: chiara.neto@sydney.edu.au

Phone: +61 2 9351 2752. Fax: +61 2 9351 3329

Abstract

The presence of nanobubbles on lubricant-infused surfaces (LIS) has so far been overlooked due to the difficulty in detecting them in such a complex system. We recently showed that anomalously large interfacial slip measured on LIS is explained by the presence of nanobubbles (Vega-Sánchez, Peppou-Chapman, Zhu & Neto, *Nat. Comms.*, **2022** *13*, pg. 351). Crucial to drawing this conclusion was the use of atomic force microscopy (AFM) force-distance spectroscopy (meniscus force measurements) to directly image nanobubbles on LIS. This technique provided vital direct evidence of the spontaneous nucleation of nanobubbles on lubricant-infused hydrophobic surfaces. In this paper, we describe in detail the data collection and analysis of AFM meniscus force measurements on LIS and show how these powerful measurements can quantify both the thickness and distribution of multiple coexisting fluid layers (*i.e.* gas and oil) over a nanostructured surface. Using this technique, thousands of force curves were automatically analyzed. The results show that the interfacial tension of the nanobubbles is reduced from $52\pm9\,\mathrm{mN\,m^{-1}}$ to $39\pm4\,\mathrm{mN\,m^{-1}}$ by the presence of the silicone oil layer.

Introduction

Gas layers dramatically affect the flow boundary conditions in microfluidic systems, reducing drag by up to 75%,[1] but are frequently overlooked when one or more dimensions are nanoscale due to the difficulty in detecting them. Nanoscale gas layers and surface nanobubbles are difficult to observe and characterize as they are too small to be quantitatively analysed using optical techniques which are typically used to study liquid-gas interfaces.[2]

Surface nanobubbles were first reported in the year 2000[2,3] and have been controversial ever since. The high Laplace pressure predicted by a nanoscale radius of curvature (*e.g.* $\Delta\mathrm{P} \approx 29\,\mathrm{atm}$ for $r = 50\,\mathrm{nm}$ and $\gamma = 72\,\mathrm{mN\,m^{-1}}$) indicates that nanobubbles should have very short lifetimes (*i.e.* on the order of $100\,\mathrm{\mu s}$[4]). However, surface nanobubbles are routinely seen to be stable on timescales of hours to days,[5] owing their stability to the fact that, despite having thickness in the range of a few tens to hundreds of nanometers, they have micrometric lateral size, which produces a flat interfacial shape with large radius of curvature. This reduces the internal Laplace pressure and allows the bubble to remain stable on the immersed surface for hours to days. For a complete review of the field, the reader is directed to the review by Lohse and Zhang.[4]

Here, we report a method to detect and map the presence of gas layers on structured hydrophobic surfaces covered with a thin layer of a hydrophobic oil. This type of surface is known as lubricant-infused surface (LIS) and has been the topic of intense research over the past decade due to their desirable properties introduced by the presence of the entrapped lubricant layer,[6] such as anti-fouling,[7–14] anti-icing,[15–19] condensation enhancement[12,20–23] and drag reduction.[24–31]

Generally, the L in LIS is used interchangeably to indicate either *liquid*[25] or *lubricant*,[17] as the most common liquids to impregnate surface structure are hydrophobic lubricants.[6] Our recent insight[32] showed that air and liquid lubricant can both coexist within a hydrophobic surface structure and both act as lubricants, leading to drag reduction. Therefore, the distinction between *liquid* and *lubricant* is important as we showed that air is the fluid providing the greatest degree of lubrication when both are present. In this work, for clarity, the two lubricants will clearly be identified as oil (which could be any water-immiscible liquid lubricant) and as a gas layer. The term 'LIS' will be used to refer to a surface initially infused with a hydrophobic liquid lubricant before being submerged in water, as we have done previously.[13,33,34]

Of particular interest is the ability of LIS to reduce interfacial drag.[24,25,31,35–38] Observed drag reduction[24,25,31] is much higher than is expected by the interfacial slip model which predicts drag reduction only when the infused oil is less viscous than the flowing liquid.[35,36,39] Our recent work showed that the presence of isolated nanobubbles on silicone oil-infused Teflon wrinkled surfaces can quantitatively explain the observed drag reduction on LIS.[32]

In this work we demonstrate that meniscus force mapping can be used to map hydrophobic oil and gas thickness simultaneously to reveal the pressence of nanobubbles on LIS. We describe AFM meniscus force measurements (a subset of AFM force-distance curves[40]) and how they can be used to detect and measure the thickness of a nanothin gas layer on top of a nanothin immiscible liquid layer, (*i.e.* a nanobubble on a submerged LIS) and show that the presence of this oil layer reduces the spring constant of the air/water interface. To our knowledge, this is the first time two liquid/gas interfaces have been quantified in a single AFM force-distance curve, and these force curves compiled to generate a time-resolved map of the spatial distribution of both phases.

Materials and Methods

Sample Preparation

Wrinkled Teflon surfaces were prepared as previously described.[13] Briefly, a shrinkable polystyrene substrate (Polyshrink$^{\text{TM}}$) was spin-coated with a thin layer ($\sim$40 nm) of Teflon AF (Chemours, 1.5% in FC-40), and then annealed in an oven (France Etuves XFM020) at 130 °C, inducing shrinking of the substrate and wrinkling of the top Teflon layer.

The as-produced wrinkles were infused by pipetting an excess of the lubricant (approx. $200\,\mu\text{L}\,\text{cm}^{-2}$) of silicone oil (10 cSt, Aldrich), spreading it, and then depleting the oil through repeated immersion through an air/water interface[33] or using a spin coater.[34]

Control over air content in working fluids

Water with different air content was used in the experiments: Milli-Q water, used as produced, and gassed water. The procedure is described in our previous publication.[32] Briefly, the oxygen concentration in water was measured using a dissolved oxygen sensor (RCY-ACO, Model DO9100) and was used to estimate the air concentration in water. Milli-Q water as produced was air-saturated at atmospheric pressure (101 kPa), and had an air content of $c_{air} \sim 23.0 \pm 0.3$ mg kg^{-1}. To produce gassed water, Milli-Q water was pressurized at 203 kPa to obtain an air content of $c_{air} \sim 44 \pm 4$ mg kg^{-1}.

Meniscus Force Measurements

AFM meniscus force measurements were all performed using the force mapping feature on an MFP-3D (Asylum, Santa Clara, CA) using hydrophobized Multi-75 probes (k = 1–7 N m^{-1}; Budget Sensors, Sofia, Bulgaria). The AFM probes are hydrophobized by depositing a thin layer of polydimethylsiloxane (PDMS) by chemical vapour deposition. The AFM probes are first cleaned using piranha solution, 3:1 sulfuric acid (98%, Ajax) : hydrogen peroxide (30%, Merck) for 5 minutes before being rinsed twice in Milli-Q water, once in ethanol, once in toluene and dried under a gentle nitrogen flow. They are then placed in a glass staining jar with a small amount of uncured PDMS (Sylgard 184, Dow Corning) and placed in an oven at 200 °C for 4 hours. After cooling, they are rinsed once more with toluene and dried under a gentle nitrogen flow. The procedure deposits 1–2 nm of PDMS (by ellipsometry).[33] Cantilever sensitivity was calculated from the contact region in 100 force curves collected on a silicon wafer and spring constants were calculated using the Asylum software by performing a thermal tune to determine resonant frequency of the cantilever prior to data collection.

A custom-made AFM sample holder is used to flood the samples with Milli-Q water *in situ*. The cell consists of a superhydrophobic barrier with a small tubing through which water can be pumped, see our previous publication for details.[33] The custom cell was used for enhanced visibility and ease of use compared to the Asylum closed liquid cell when flooding a sample with water. This was important in previous work, but any underwater cell is sufficient to image nanobubbles using the technique described herein.

Force maps typically have 64x64 pixels and lateral size of 1–4 µm. All data was analysed using Python 3 using packages included in the Anaconda scientific computing distribution.[41] Raw force curve data was exported to ASCII format before being loaded in the Python script and analysed using the algorithm described herein. All code used in this work is available online.[42]

Results and Discussion

The detection of a thin gas layer sandwiched between the oil layer and the bulk water depends on detecting two features seen in AFM force-distance measurements. Oil layers are identified by a sharp negative deflection of the AFM cantilever, due to meniscus formation (hence the name, meniscus force measurements)[34,43–47] and gas layers are identified through the positive deflection of the cantilever.[48–52] Both these features are seen in the example force curve in Figure 1c, which was captured over an area identified as having both layers. Here, a positive deflection (*i.e.* a force pushing the AFM tip away from the surface) is seen at larger separations and a negative deflection (*i.e.* a force drawing the tip towards the surface) is seen a smaller separations, corresponding to the nanobubble and oil layer, respectively.

In this work, only extension curves were used and are presented, as the forces of interest occur as the tip moves towards the surface. Unless specified otherwise, all data was collected on a LIS composed of wrinkled Teflon infused with 10 cSt silicone oil.[13,32]

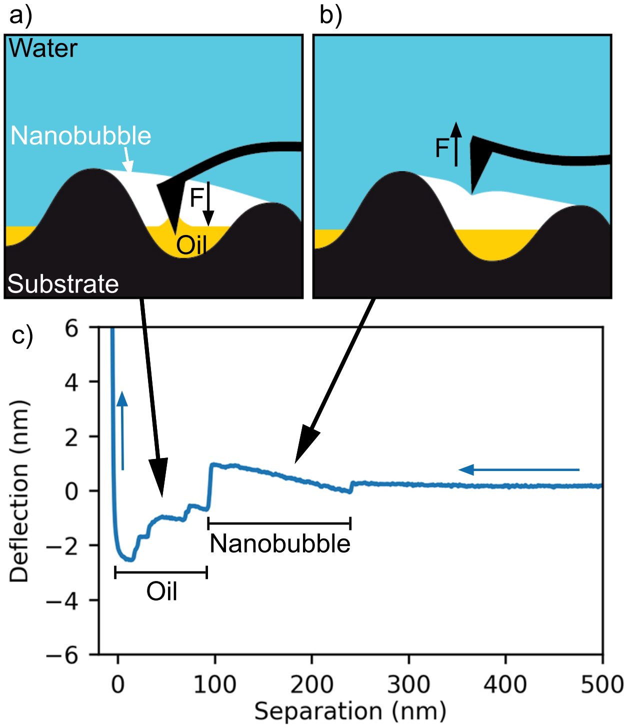

Figure 1: Schematic showing an AFM tip approaching a nanobubble over a layer of oil: both the (a) oil thickness and (b) the nanobubble thickness (not to scale) are measured due to the opposite forces they exert on the AFM tip. c) Example of an experimentally obtained force curve from which the nanobubble thickness and oil thickness are extracted.

Meniscus Force Measurements

Meniscus force measurements are a subset of AFM force spectroscopy in which the dominant force on the cantilever is due to the formation of a liquid meniscus around the AFM tip. In contrast to the case where the AFM tip first encounters the solid surface (see Figure 2a), when the AFM tip first contacts the air/liquid interface, a liquid meniscus forms around the tip and pulls down the cantilever towards the surface (see Figure 1a), causing a rapid negative deflection (see Figure 2b). The distance between this so-called 'jump-in' and the position where the AFM tip contacts the hard substrate underneath is the thickness of the liquid film, and can be revealed with nanoscale accuracy.[34,43–47] A detailed discussion on the accuracy of the technique is provided.[43–45]

An advantage of this technique is that it is agnostic to the identity of the two phases. As long as the interfacial energy of the liquid is sufficiently high to observe a jump-in when the AFM tip touches it, the interface will be detected in the force curve. As a result, we have used this technique to map the thickness of a hydrophobic oil layer both in air[34,53] and underwater[33] as the water/oil interface has sufficient wetting contrast to produce the required jump-in. Figure 2b shows the shape of a typical force curve of a thin oil film underwater where a sharp negative deflection is seen at about 120 nm separation, before a sharp positive deflection when the tip contacts the underlying substrate.

Force-Distance Curves on Surface Nanobubbles

Due to their nanoscale dimensions, nanobubbles are not routinely studied using optical techniques typical in the study of larger gas bubbles. Instead, the nanoscale nature of AFM measurements has made it the technique of choice for the study of nanobubbles using both tapping mode and force-distance spectroscopy.[2,4,5,54]

Nanobubbles imaged using AFM are typically identified as small round protrusions on an otherwise flat substrate.[2] These images are produced using a typical imaging technique such as tapping mode or with a force-based method such as PeakForce QNM[54] where the cantilever's stiffness must be sufficiently low so that the tip does not penetrate the bubble as these stiffness maps are calculated from the contact region of the force curve. On structured surfaces, nanobubbles will exist within the surface roughness and may not protrude in the same way as on a flat surface. Additionally, in the case of a superhydrophobic surface, there may be a thin gas which covers the surface entirely, giving a flat topography image. Instead, force spectroscopy does not rely on topographic identification, only the forces experienced by the cantilever.

In AFM force-distance measurements, nanobubbles are identified through a characteristic positive deflection (pushing the tip away from the substrate, see Figure 1b) due to deformation of the air/water interface.[48,51] Figure 2c shows the shape of a typical force curve taken on a nanobubble, showing a section of force curve with a positive gradient between the zero force baseline and the hard contact point. Many publications have confirmed that this particular feature in the force curve shape is due to nanobubbles.[5,48–52]

Imaging Nanobubbles on LIS

The two types of force curves described above combine when a gas layer is present on top of an oil layer underwater. In its approach towards the surface, the tip first deflects away due the deformation of the bubble and then towards the substrate due to meniscus formation when it contacts the oil layer, see Figure 2d. The first point at which the positive deflection occurs is used to indicate the top of the gas layer and the first point of the negative deflection indicates the top of the oil layer (see Figure S1). This interpretation may lead to small under- or overestimation of the layer thickness in certain cases. These effects are explored more below. The steps present in the attractive part of the force curve are due to the stick-slip motion of the oil/water interface; if the contact line remains temporarily pinned on the surface of the tip, the force does not increase gradually and smoothly, but in steps, as previously shown.[55]

The process of imaging nanobubbles on LIS is similar to that of imaging the oil layer underwater,[33] with most of the difference consisting in the data analysis.

The four expected configurations of fluid layers and example force curves for an immersed LIS under static conditions are shown in Figure 2: water on substrate, water on oil on substrate, water on gas on substrate, water on gas on oil on substrate. We do not observe a thick layer of oil on a nanobubble, and indeed a thick layer is not expected to be stable as the

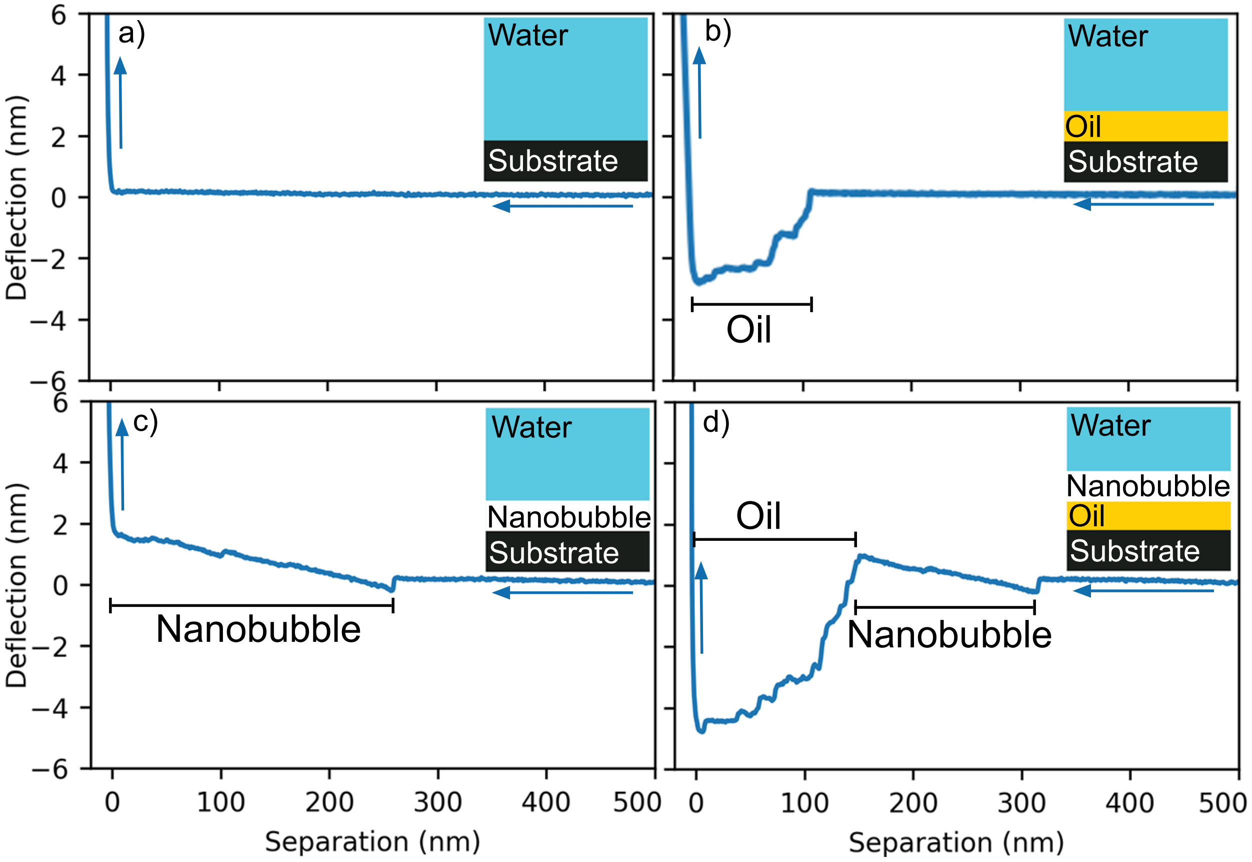

Figure 2: Example of the four types of force curves observed on silicone oil-infused Teflon LIS under Milli-Q water. Extension force curve as the AFM tip comes in contact with a) bare solid substrate under water; b) an oil film on the solid substrate under water; c) a gas layer on the solid substrate under water; d) a gas layer on an oil layer on the solid substrate under water.

static pressure (acting down, from the water above) and Laplace pressure (acting up, from the nanobubble) would destabilise the oil layer.[56] On the other hand, a nano-thin film ($\lesssim 5\,\mathrm{nm}$) of oil is expected to cloak the nanobubble due to the positive spreading parameter of oil at the water/air interface, but was not directly detected as an additional jump-in before the the tip contacts the bubble. Although there is a small jump-in seen in Figure 2c,d, this is due to the gas layer forming a small meniscus on the AFM tip and not due to an oil layer. However, a jump-in is not always observed upon approach to a nanobubble due to differences in the tip surface chemistry: a slightly more hydrophilic AFM tip approaching a nanobubble will not register a jump-in feature as a gas meniscus does not form on a hydrophilic tip.[51] Figure S2 shows two force curves from an experiment using a different AFM tip (but, in principle, with the same hydrophobic treatment) that do not show a jump in. However, as discussed below, the spring constant of the bubble is reduced by the presence of a lubricating oil layer.

The time required for the formation of nanobubbles is dependent on the gas content in the water. Nanobubbles appeared faster in water gassed with air (*e.g.* for water air content $c_{air} \sim 44 \pm 4\ \mathrm{mg\,kg^{-1}}$ they appeared instanteously, see Figure 5e), while they appeared a few hours after immersion in plain Milli-Q water, which was saturated at atmospheric pressure ($c_{air} \sim 23.0 \pm 0.3\ \mathrm{mg\,kg^{-1}}$). Figure 5a-d show the nucleation of a nanobubble on a surface through successive mapping of the same location. Each map took ∼35 minutes and the bubble appeared between successive maps. The surface was submerged for a total 2-3 hours in the absence of flow before the nanobubble appeared.

AFM Probe Considerations

The choice of tip shape and chemistry is important to achieving a clear image of both the oil and the gas layer. In AFM mapping techniques, a sharp tip is generally preferred as it gives maximum spatial resolution, but for meniscus force measurement a thinner tip decreases the force on the cantilever as the force is determined by the length of the contact line.[43,55] As a result, there is a balance between spatial resolution and force resolution.

Similarly, cantilever spring constant is critical to successful meniscus force measurements. A low spring constant is needed for the cantilever to deflect due to meniscus formation and to deflect from the reaction force caused by nanobubble deformation. Additionally, a lower spring constant allows for a sharper tip to be used. However, the spring constant cannot be too low (*e.g.* a contact mode probe), as the cantilever is not able to break free from the meniscus during retraction. Here, force modulation AFM probes with a spring constant of $\sim 5\,\mathrm{N\,m^{-1}}$ and a sharp tip were used, as these provide sufficiently large deflection values with good spatial resolution.

For imaging hydrophobic oil layers, tip chemistry determines the magnitude of the force exerted by the meniscus (determined by the length of the contact line). The fluid layer that forms the meniscus should preferentially wet the tip for a meniscus to form. In air, this is trivial as almost all fluids wet the high surface energy silicon nitride which makes up most AFM tips. Underwater, this is less simple as a hydrophilic tip may be wet preferentially by the water and therefore a clear jump-in from a hydrophobic oil might not be apparent. Here, the tip was hydrophobized with a thin layer of PDMS to ensure a wettability contrast between the water and the thin oil layer. An unmodified tip was seen to work initially, but the image quality deteriorated quickly, leading to the loss of jump-in.

For imaging nanobubbles, the opposite is required. The thickness of a nanobubble is better imaged using a hydrophilic tip as the tip is less likely to penetrate into the bubble so all changes in deflection are due to nanobubble deformation.[51] A hydrophobic tip still shows deflection due to nanobubble deformation and it also shows signs of meniscus formation as the tip contacts the nanobubble. This aspect is discussed further below.

Data Analysis

The key to using AFM meniscus force measurements for mapping of multiple layers was the automated data analysis with feature recognition to determine the points at which the tip contacts different interfaces. This section describes the logic used by our Python script to calculate the thickness of both the gas and oil layer from the collected force curves.

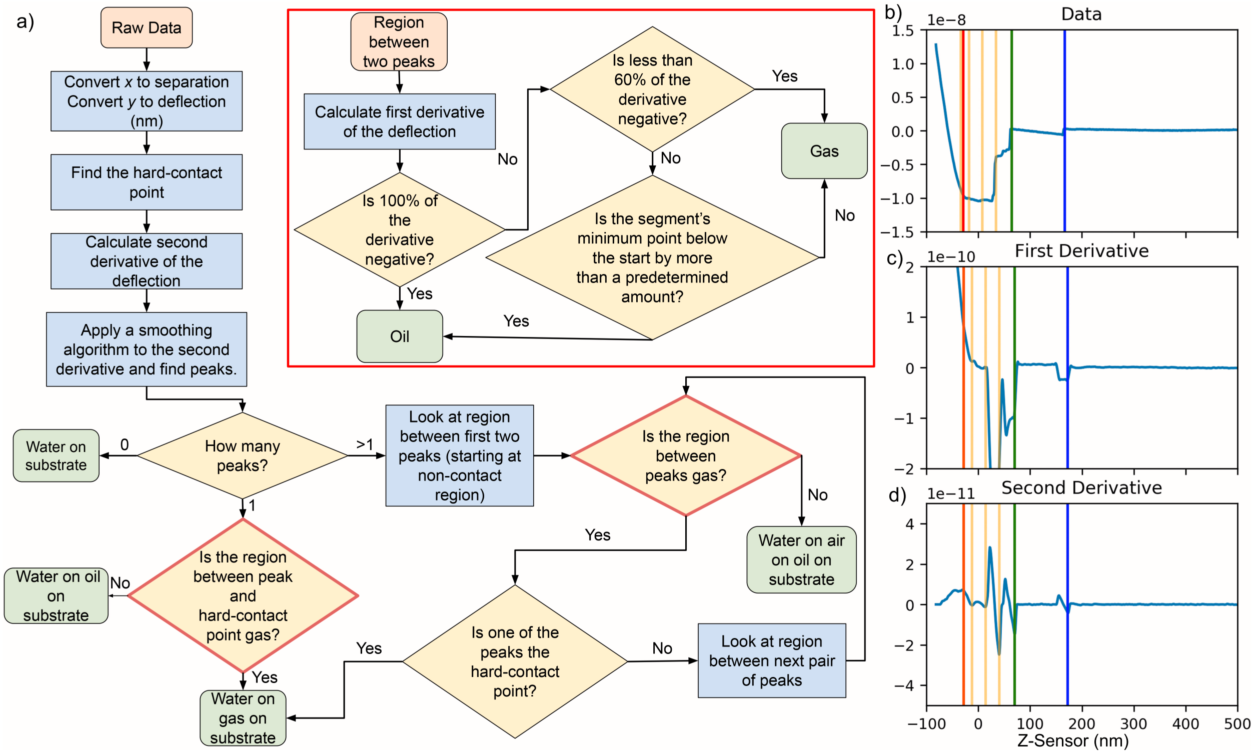

Figure 3: a) Flowchart showing the process used to characterise each force curve in the raw force map data. The red rectangular inset shows the logic used in the decision nodes with a red outline to determine whether the data between two features of a force curve is gas or lubricant. See GitHub[42] for code. b) Raw force curve data of cantilever deflection (y scale is in m) as function of z-displacement for an example force curve. c) The first derivative of b) (y scale is $\mathrm{m\,nm^{-1}}$). d) The second derivative of b) (y scale is $\mathrm{m\,nm^{-2}}$). The orange vertical lines represent negative peaks picked from the second derivative. The red, green, and blue lines represent the location of the substrate, the top of the oil and the top of the nanobubble, respectively.

For an underwater LIS there are four possible scenarios for the fluid layers each force curve may encounter (see Figure 2):

a) Water on substrate;

b) Water on oil on substrate;

c) Water on gas on substrate;

d) Water on gas on oil on substrate;

In our previous work,[33,34,53] the script only detected an oil layer (*i.e.* scenarios (a) and (b)), where only two key points needed to be detected: the jump-in and hard contact point. As a result of the added complexity added by the gas layer, a completely new detection algorithm was used here to identify all four of these scenarios. The features associated with the gas layer are less pronounced than the oil layer, and so a lower threshold for detection of features needed to be implemented.

Here, the algorithm utilises automated peak finding to find areas of rapid changes in the gradient of the deflection and the fact that the gradient of the deflection is opposite in sign when the tip is in contact with a nanobubble versus when in contact with a meniscus due to an oil layer. The general procedure used in the script is (see also Figure 3a):

- Convert piezo movement data to separation, and photo diode signal to deflection, using sensitivity of cantilever calculated from compliance region measured on a hard surface.
- Find the hard-contact point by finding the first point with a substantial change in gradient in the contact region of the extend curve.
- Calculate the second derivative of the whole data and apply a smoothing algorithm to the y-data (deflection).
- Use a peak finding algorithm to find negative peaks in the smoothed second derivative (orange lines in Figure 3b-d).
- If no peaks are detected, there is no oil or gas (*i.e.* case in Figure 2a)
- If one peak is detected, then the region between it and the hard contact point can either be oil or gas. Check if gas or oil using the algorithm outlined below. (*i.e.* case in Figure 2b,c).
- If multiple peaks are detected, each segment between two peaks is checked to see if it is gas or not using the algorithm outlined below. The first segment identified as oil

demarcates the boundary between the gas and oil (*i.e.* case in Figure 2d). If no oil is detected before reaching the hard contact point, then there is no oil present and the layer is entirely gas (i.e case in Figure 2c).

To determine whether a segment between two of the negative peaks identified in the second derivative is gas or oil, the following algorithm is used (see also inset within the red box in Figure 3a):

- If 100% of the first derivative is negative – the portion is oil. This is because the force acting on the cantilever is proportional to the length of the contact line and this force always increases (due the triangular shape of the tip) as the tip moves towards the surface – causing the deflection to become more negative.
- If more than 60% of the points of the first derivative are negative and the end is lower than the start by a threshold deflection (0.5 nm in this work, determined using trial and error), then portion is considered oil. Otherwise, it is gas.

The script then outputs the height of the hard contact point (absolute height from z-sensor data) and the thickness of the oil or gas layers found (calculated as the distance between relevant peaks in separation). Figure 4a shows a map with example forces curves and their corresponding location in the map. The force curves (Figure 4b-g) also show the features located by the algorithm described above (blue = start of gas layer, green = start of oil layer, and red = start of the substrate).

Validation

The automated analysis was validated by a manual review of analysed force curves to judge if the script had picked the correct locations for the start of gas and oil layers. Force curves from multiple maps were plotted with the vertical lines showing the interfaces as picked by the script as in Figure 3b and Figure 4 and were judged by eye if these were correct. A total of 494 force curves were selected at random and 93% of them were judged to be correctly fitted. Potential reasons for incorrect fitting are discussed below.

Data Visualisation

As shown in Figure 4, the data is presented as multi-panel maps showing the spatial distribution of the different phases detected. First, the sample topography is presented (extracted from the hard contact point of the force curves). Then maps of the oil thickness and the gas thickness are presented separately. Both oil and gas thickness are presented as non-linear contours where colours are evenly spaced at thickness of 2 nm up to 20 nm and then contours of 150 nm, 300 nm and >300 nm to give an indication of distribution of both thin layers and thick layers. This method of presentation was selected as it gives the ability to easily attribute the effect of topography on the distribution of either the liquid or the gas layer.

Cross sectional profiles of these maps can be extracted to visualise the shape of the interfaces, as shown in Figure 5, in which color was added to the line profiles to highlight the different fluid layers. Each cross section corresponds to the cyan line in the adjacent maps. As mentioned above, part (a) and part (b) in Figure 5 are sequential maps (taken approximately 35 mins apart) of the same surface before and after a nanobubble nucleates. Figure 5e,f shows a cross sections from the LIS in Figure 4 while Figure 5g,h shows gas pockets on an immersed superhydrophobic surface (Teflon wrinkles with no oil present) in a partially-collapsed Cassie state. Despite the apparently high resolution of the contact line of the mapped interfaces, the local contact angle values cannot be estimated, as discussed below.

Additional parameters are easily calculated from the resulting maps, such as the position of the water interface or the mean curvature of this interface, see Figure S3.

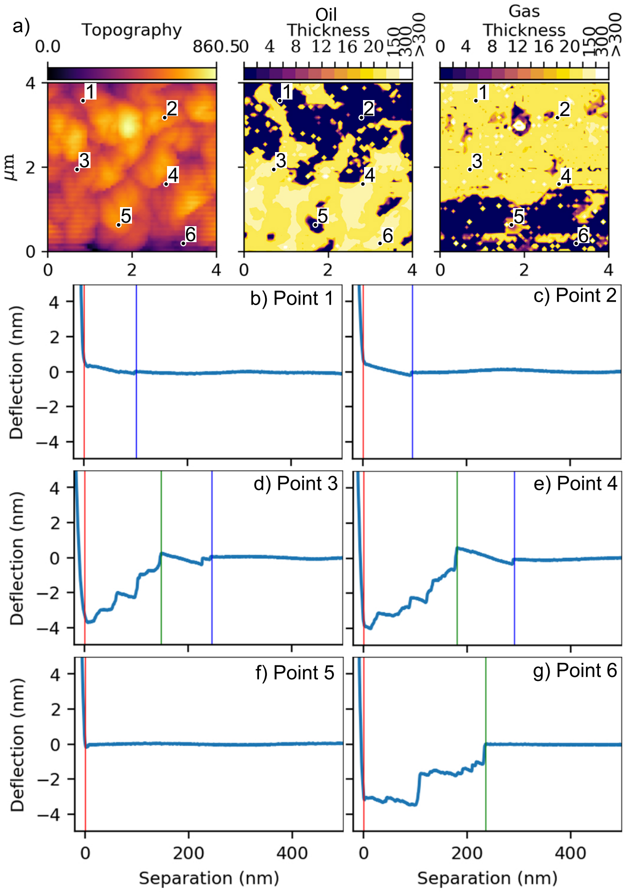

Figure 4: a) Map of a nanobubble on a LIS with (b-g) example force curves shown for points with different fluid layers. The map (a) is presented with three panels showing the topography of the underlying Teflon wrinkles (left), the thickness of the oil (middle) and the thickness of the gas (right); the units of all colour scales is nm. Points 1 and 2 show an example of a nanobubble directly on the substrate. Points 3 and 4 show an example of a nanobubble on oil. Point 5 shows an example of the water directly contacting the substrate and point 6 shows an example of water contacting the oil. The vertical lines in the force curves show where the script has found the start of the different fluid layers, blue = start of gas layer, green = start of oil layer, and red = start of the substrate.

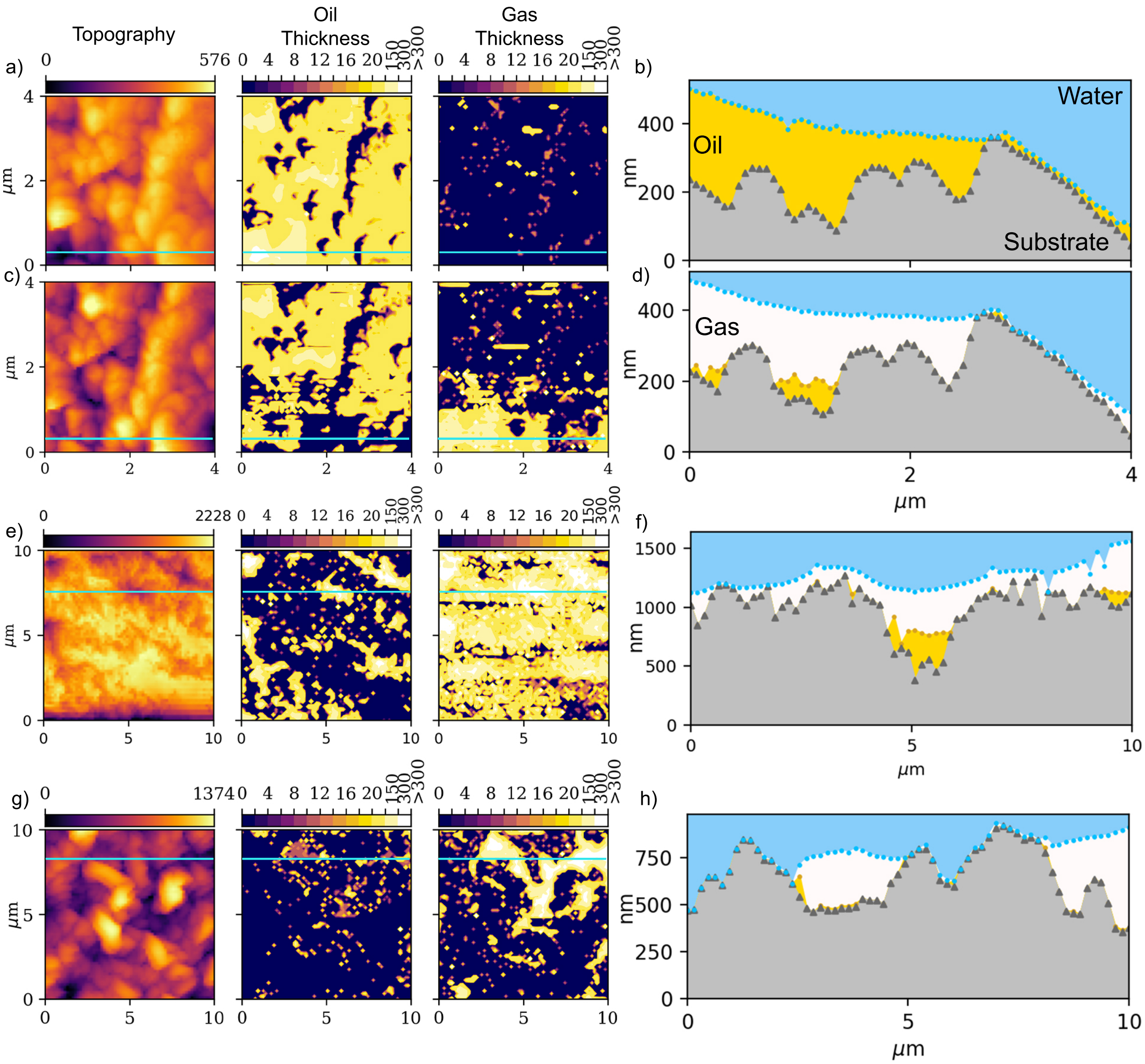

Figure 5: AFM force maps showing oil and gas thickness (a, c, e, g) with cross sections (b, d, f, h) corresponding the cyan lines in the maps. The unit of all colour scales is nm. The marker symbols in the cross sections represent points at which the height was measured, and colors were added to help visualise the different layers. a) and b) are successive maps on the same area of the surface, showing the appearance of a nanobubble *in situ*. The force curves were collected and analysed using the same parameters. e, f) Example of a LIS submersed in gassed water ($c_{air} \sim 44 \pm 4$ mg kg^{-1}) imaged immediately after submersion. g, h) A superhydrophobic surface in MilliQ water (nanowrinkled Teflon substrate without any silicone oil applied) showing a partially collapsed Cassie state. The non-zero measurements of oil thickness at multiple points on this map are a result of the feature detection algorithm not always being able to discern the difference between oil and gas or the particular force curve being noisy.

Limitations and Sources of Error

There are several limitations and sources of error related to this technique but their importance is limited by the mapping nature which allows individual errant pixels to be ignored.

The accuracy of the measured thickness depends on many factors and is not uniform for all film thicknesses. Very thin (<5 nm) films of either gas or oil are difficult to both detect and distinguish. The technique's ability to detect a nanoscale film increases with increasing film thickness, as thicker films (either gas or oil) produces a greater deflection while films of just a few nanometers produce a deflection on the same order as measurement noise. As a result, regions of zero film thickness may contain undetected films of a few nanometers.

Automated feature detection exacerbates this limitation as there is a trade-off between sensitivity (*i.e.* detecting smaller deflections) and avoiding false detection at large separations (*e.g.* more than 100 nm from the first interface as in Figure 6d). The noise present in the oil and gas thickness maps in Figure 4 is the result of imperfect fitting that occurs due to higher feature detection sensitivity. Using a thicker tip would reduce this effect but, as mentioned above, would reduce lateral resolution. Slightly thicker films (up to tens of nm) can be detected but with fewer data points to judge whether the feature in the force curve is due to oil or gas, the script is prone to mislabelling these. Figure 6a,b shows examples of two features at small separations with deflections $\sim$1 nm which are ambiguous and were identified as different features by the script, despite being adjacent pixels in the map.

Ideally, if the AFM tip is hydrophilic, the air/water interface would not form a three-phase contact line with tip, ensuring that all positive deflection is due to the deformation of the interface. If there is a three-phase contact line, ideally it would be pinned to the same spot of the tip through the entire range of motion of the force curve. This is not always the case and the contact line may jump producing a discontinuity in the gas portion of the force curve as in Figure 6e. In this particular case, the analysis script has erroneously picked this movement of the contact line to be the start of the oil layer. See also Figure S4 for an example of a force curve where the contact line jumped multiple times in the force curve.

As the AFM tip used here is hydrophobic, it is expected to form a three-phase contact line with the air/water interface, which is confirmed by the small jump-in seen at the start of the gas layers.

The presence of a nano-thin layer of oil spread on the AFM tip cannot be excluded, which would increase the measured thickness of the oil layer. As with our previous publications, this does not seem to be an issue as there are multiple cases where no oil thickness is detected either under a nanobubble or elsewhere (*e.g.* Figure 2a,c). However, the lack of sensitivity to very thin films (<5 nm) described in the previous paragraph may hide the effects of such a film.

The thickness of the oil layer may be overestimated if long range van der Waals attraction between the tip and an interface draws the interface up to 'meet' the tip.[46] In our previous publication, this effect was suppressed by sufficiently fast scan rate in the force curve.[34] As a result, here the fastest scan rate possible on our AFM (2 Hz) was used to ensure this effect is minimized. This deformation will also effect the gas layer, with the air/water interface deforming to meet the tip, especially for a hydrophobic tip.[51] As a result of this deformation, Walczyk & Schönherr[51] define the top of the a nanobubble measured with a hydrophobic tip to be where the force curve crosses zero deflection after the initial jump-in. Here, the potential long-range attraction of the air/water interface was ignored, due to the high scan rates used and because this correction would cause the calculated gas height to depend on the quality of the baseline correction. Additionally, Walczyk & Schönherr's definition of the top of a nanobubble assumes that the AFM tip only contacts the bubble with minimal contact line at zero deflection (*i.e.* the only force on the cantilever is due to nanobubble deformation), which is impossible given the fact that a jump-in is seen, signifying meniscus formation and a non-trivial contact line.

There are limitations of the experimental setup which contribute noise in the maps. Force curves collected under water are particularly sensitive to vibrations, as they can be transmitted through the liquid to the cantilever. This means that a higher proportion of

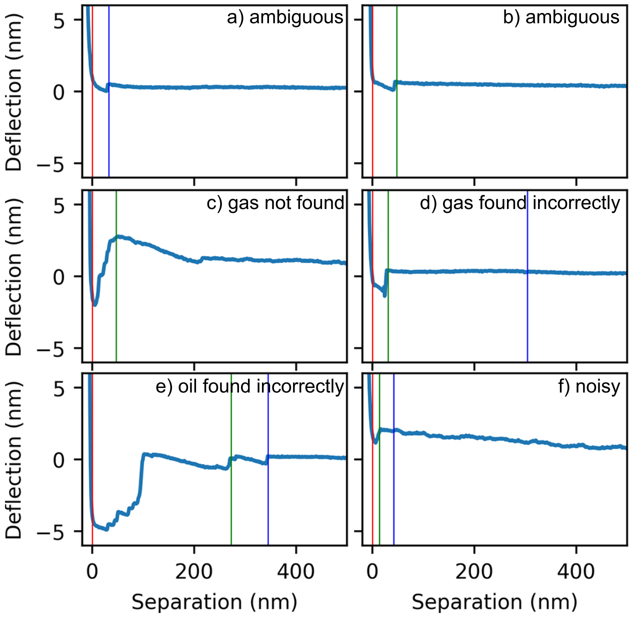

Figure 6: Force curves showing the limitations of the automatic feature detection script presented in this work. Vertical lines indicate where the analysis script found an interface with blue = start of gas layer, green = start of oil layer, and red = start of the substrate. a,b) Two force curves obtained on adjacent locations, where the identity of the feature is ambiguous, with the script identifying in (a) a gas layer and in (b) a oil layer; c) an example of the script not detecting gas; d) an example of the script incorrectly detecting the gas/water interface; e) an example of the script incorrectly detecting the oil/gas interface instead of more gas; f) an example of a noisy force curve, likely due to vibrations.

force curves are noisy throughout their entire range of motion, compared to the same force measurement in air, leading to incorrect feature detection (see Figure 6c/f).

The cross sections generated from the map cannot be used to quantify contact angle values as the interface is 3-dimensional and contributions from in-plane and out-of-plane features are impossible to account for. Additionally, the shape of the interface may be slightly deformed due van der Waals interactions not being consistent across the surface.

Measurement of nanobubble spring constant

An outstanding question is whether the nanobubbles that appear on LIS are covered in oil or not. In our system, which uses silicone oil, the air/water interface is predicted to both be covered and not covered depending on the theoretical framework used. Long-range van der Waals interactions approximated using the non-retarded Hamaker constants (estimated using Lifshitz theory) of the system predict that a thin film of silicone oil on the air water/interface is unstable.[33] However, the spreading parameter ($S = \gamma_{WG} - (\gamma_{WL} + \gamma_{LG}) \approx 72 - 35 - 19 \approx 18\,\mathrm{mN\,m^{-1}}$) is positive, indicating that the interface is expected to be covered with silicone oil to lower the overall energy of the system.[42]

Given these contradictory predictions, we can use the technique outlined here to directly measure the spring constant of the bubbles on a surface with and without silicone oil to determine if the bubble interface is covered or not. The presence of a thin layer of silicone oil will lower the interfacial tension and thereby lower the spring constant of the bubble, which is approximately equal to the interfacial tension.[5,49,57] The gradient of the deflection vs separation for the nanobubble is equal to the negative of the ratio of the nanobubble spring constant to the cantilever spring constant.[5,57] In other words, the nanobubble spring constant is equal to the gradient of the nanobubble portion of the force vs separation graph.

The spring constant of detected gas layers was measured by fitting a line to the portion of the force vs separation graph identified as gas (collected with a cantilever with known spring constant). Only gas layers of thickness 30–500 nm were considered to exclude the

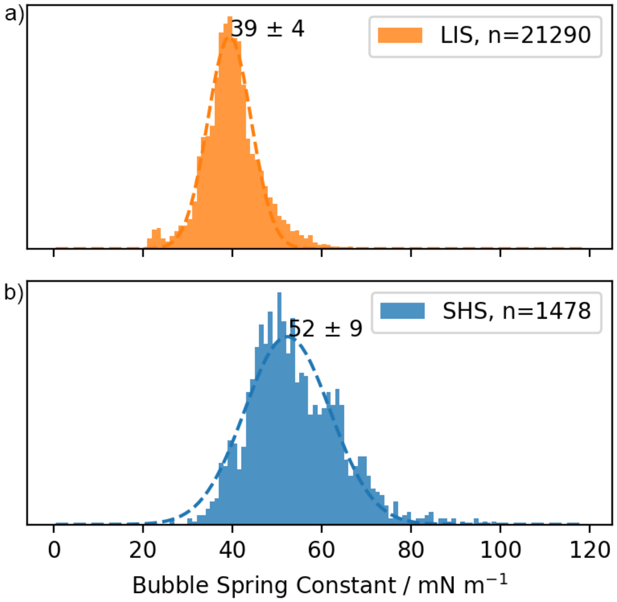

Figure 7: Histogram showing the distribution of measured spring constants of the gas layer from individual force curves on a)lubricant-infused surfaces (LIS, $n = 21290$) and b) superhydrophobic surfaces (SHS, $n = 1478$) where n is the number of force curves analysed. Fitting Gaussian functions to these distributions gives a spring constant value for the gas layer on LIS of 39±4 mN m^{-1} and for nanobubbles on SHS of 52±9 mN m^{-1}.

errors discussed in the previous section and only force curves with a linear fit $R^2 > 0.98$ were included to ensure that the deflection was due to only the deformation of the gas layer.

Figure 7 shows the results collated from thousands of force curves on multiple Teflon wrinkled surfaces, both with infused silicone oil (LIS) and without silicone oil (superhydrophobic, SHS), and shows that bubble spring constant values fall within a single distribution in each case giving a spring constant value for the gas layer on LIS of 39±4 mN m^{-1} and for nanobubbles on SHS of 52±9 mN m^{-1}.

The lower spring constant detected on the LIS indicates that the presence of lubricant lowers the interfacial tension of the air/water interface. As a result, this suggests that although a film is not predicted to be stabilised through intermolecular interactions, there is sufficient silicone oil present to affect the measurement. From these measurements, we cannot say whether this oil exists in a stable (or meta-stable) film or if the silicone oil is deposited at the interface by the AFM tip in each force curve.

As previously mentioned, the spring constant of a nanobubble is approximately equal to its interfacial tension,[5,49,57] but the results here are not close to the expected values of $72\,\mathrm{mN\,m^{-1}}$ on the SHS and $54\,\mathrm{mN\,m^{-1}}$ on the LIS (effective surface tension of an air/water interface covered in a thin lubricant film;[56] $\gamma_{eff} = \gamma_{WL} + \gamma_{LG} = 35 + 19 = 54\,\mathrm{mN\,m^{-1}}$). However, given the rough nature of the substrates use in this work, the bubbles probed are not hemispherical caps (see Figure 5,Figure S3, Figure S5) such as in other work[5,27,48,50,51,58] and, as a result, our system more closely resembles that of a bounded flat interface which is expected to give an effective spring constant lower than the interfacial tension.[59] De Baubigny *et al.*, found that a cylindrical AFM tip gave a spring constant for a meniscus lower than the interfacial tension, and that the spring constant was dependent on the lateral extension of the meniscus.[59] Given that the wrinkled surface used here have features of varying size from a few micrometers to tens of micrometers, as measured previously,[32] and that the nanobubbles can bridge more than one wrinkle, it is difficult to obtain a quantitative agreement between our measured interfacial tension and the De Baubigny model for a confined meniscus. Both the size of the bubble and the local contact angle of the gas/water interface with the tip affect the exact value of interfacial tension obtained (see Supplementary Text, Figure S6, Figure S7, Figure S8). What is certain is that the measured spring constant of the water/gas interface on LIS is lower than that in SHS of the same topography, that the values obtained are sensible, and that the decrease can be explained with the presence of silicone oil contamination. Future measurements of interfacial tension of air/water interfaces on regular microstructured surfaces will enable the quantitative verification of the De Baubigny model.

Conclusion

In summary, we have shown that a single AFM force-distance curve can capture the thickness and distribution of both a gas layer and an immiscible liquid layer underwater simultaneously. By mapping a surface with force curves and analysing the data automatically, the thickness of the gas and the immiscible liquid are both spatially resolved. This is an exciting new technique to study the nanoscale interfacial properties of nanobubbles and here we have shown that the spring constant of nanobubbles is reduced by the pressence of silicone oil. There are still many outstanding questions related to the nucleation of nanobubbles on LIS including how substrate topography, surfactant/ion concentration, flow and static pressure influence nanobubble nucleation and stability. This force mapping technique will enable detailed studies of these parameters and reveal whether the presence of nanobubbles influences other properties of LIS attributed to the lubricant layer and how the lubricant layer influences the physical properties of the nanobubble.

Acknowledgement

SPC acknowledges the Australian Government Research Training Program (RTP) for support. CVS acknowledges the Costa Rican Ministry of Science and Technology and Tecnológico de Costa Rica for funding. CN acknowledges funding from the Australian Research Council through the Future Fellowship scheme (FT180100214).

Supporting Information Available

The Supporting Information is available free of charge on the ACS Publications website. Additional data includes: a map with additional metrics, example of a force curve with a moving contact line, and calculation of reduced spring constant of a bounded meniscus.

References

(1) Lee, C.; Choi, C.-H.; Kim, C.-J. Superhydrophobic drag reduction in laminar flows: a critical review. *Exp. Fluids* **2016**, *57*, 1–20.

(2) Alheshibri, M.; Qian, J.; Jehannin, M.; Craig, V. S. A History of Nanobubbles. *Langmuir* **2016**, *32*, 11086–11100.

(3) Ishida, N.; Inoue, T.; Miyahara, M.; Higashitani, K. Nano bubbles on a hydrophobic surface in water observed by tapping-mode atomic force microscopy. *Langmuir* **2000**, *16*, 6377–6380.

(4) Lohse, D.; Zhang, X. Surface nanobubbles and nanodroplets. *Rev. Mod. Phys.* **2015**, *87*, 981–1035.

(5) Zhang, X. H.; Maeda, N.; Craig, V. S. Physical properties of nanobubbles on hydrophobic surfaces in water and aqueous solutions. *Langmuir* **2006**, *22*, 5025–5035.

(6) Peppou-Chapman, S.; Hong, J. K.; Waterhouse, A.; Neto, C. Life and death of liquid-infused surfaces: a review on the choice, analysis and fate of the infused liquid layer. *Chem. Soc. Rev.* **2020**, *49*, 3688–3715.

(7) Epstein, A. K.; Wong, T. S.; Belisle, R. A.; Boggs, E. M.; Aizenberg, J. Liquid-infused structured surfaces with exceptional anti-biofouling performance. *Proc. Nat. Acad. Sci. USA* **2012**, *109*, 13182–13187.

(8) Sunny, S.; Vogel, N.; Howell, C.; Vu, T. L.; Aizenberg, J. Lubricant-Infused Nanoparticulate Coatings Assembled by Layer-by-Layer Deposition. *Adv. Funct. Mater.* **2014**, *24*, 6658–6667.

(9) Maccallum, N.; Howell, C.; Kim, P.; Sun, D.; Friedlander, R.; Ranisau, J.; Ahanotu, O.; Lin, J. J.; Vena, A.; Hatton, B.; Wong, T. S.; Aizenberg, J. Liquid-Infused Silicone As a Biofouling-Free Medical Material. *ACS Biomater. Sci. Eng.* **2015**, *1*, 43–51.

(10) Sotiri, I.; Overton, J. C.; Waterhouse, A.; Howell, C. Immobilized liquid layers: A new approach to anti-adhesion surfaces for medical applications. *Exp. Biol. Med.* **2016**, *241*, 909–918.

(11) Ban, G. H.; Lee, J.; Choi, C. H.; Li, Y.; Jun, S. Nano-patterned aluminum surface with oil-impregnation for improved antibacterial performance. *LWT-Food Sci. Technol.* **2017**, *84*, 359–363.

(12) Al-Sharafi, A.; Yilbas, B. S.; Ali, H. Heat Transfer and Fluid Flow Characteristics in a Sessile Droplet on Oil-Impregnated Surface Under Thermal Disturbance. *J. Heat Transfer* **2017**, *139*, 14.

(13) Ware, C. S.; Smith-Palmer, T.; Peppou-Chapman, S.; Scarratt, L. R.; Humphries, E. M.; Balzer, D.; Neto, C. Marine Antifouling Behavior of Lubricant-Infused Nanowrinkled Polymeric Surfaces. *ACS Appl. Mater. Interf.* **2018**, *10*, 4173–4182.

(14) Wang, Y.; Zhao, W.; Wu, W.; Wang, C.; Wu, X.; Xue, Q. Fabricating Bionic Ultraslippery Surface on Titanium Alloys with Excellent Fouling-Resistant Performance. *ACS Appl. Bio. Mater.* **2019**, *2*, 155–162.

(15) Kim, P.; Wong, T. S.; Alvarenga, J.; Kreder, M. J.; Adorno-Martinez, W. E.; Aizenberg, J. Liquid-infused nanostructured surfaces with extreme anti-ice and anti-frost performance. *ACS Nano* **2012**, *6*, 6569–6577.

(16) Kreder, M. J.; Alvarenga, J.; Kim, P.; Aizenberg, J. Design of anti-icing surfaces: smooth, textured or slippery? *Nat. Rev. Mater.* **2016**, *1*, 15.

(17) Subramanyam, S. B.; Rykaczewski, K.; Varanasi, K. K. Ice adhesion on lubricant-impregnated textured surfaces. *Langmuir* **2013**, *29*, 13414–13418.

(18) Yamazaki, T.; Tenjimbayashi, M.; Manabe, K.; Moriya, T.; Nakamura, H.; Nakamura, T.; Matsubayashi, T.; Tsuge, Y.; Shiratori, S. Antifreeze Liquid-Infused Surface with High Transparency, Low Ice Adhesion Strength, and Antifrosting Properties Fabricated through a Spray Layer-by-Layer Method. *Ind. Eng. Chem. Res.* **2019**, *58*, 2225–2234.

(19) Wong, W. S. Y.; Hegner, K. I.; Donadei, V.; Hauer, L.; Naga, A.; Vollmer, D. Capillary Balancing: Designing Frost-Resistant Lubricant-Infused Surfaces. *Nano Lett.* **2020**, *20*, 8508–8515.

(20) Anand, S.; Rykaczewski, K.; Subramanyam, S. B.; Beysens, D.; Varanasi, K. K. How droplets nucleate and grow on liquids and liquid impregnated surfaces. *Soft Matter* **2015**, *11*, 69–80.

(21) Preston, D. J.; Lu, Z.; Song, Y.; Zhao, Y.; Wilke, K. L.; Antao, D. S.; Louis, M.; Wang, E. N. Heat Transfer Enhancement During Water and Hydrocarbon Condensation on Lubricant Infused Surfaces. *Sci. Rep.* **2018**, *8*, 540.

(22) Sett, S.; Sokalski, P.; Boyina, K.; Li, L.; Rabbi, K. F.; Auby, H.; Foulkes, T.; Mahvi, A.; Barac, G.; Bolton, L. W.; Miljkovic, N. Stable Dropwise Condensation of Ethanol and Hexane on Rationally Designed Ultrascalable Nanostructured Lubricant-Infused Surfaces. *Nano Lett.* **2019**, *19*, 5287–5296.

(23) Kajiya, T.; Wooh, S.; Lee, Y.; Char, K.; Vollmer, D.; Butt, H. J. Cylindrical chains of water drops condensing on microstructured lubricant-infused surfaces. *Soft Matter* **2016**, *12*, 9377–9382.

(24) Solomon, B. R.; Khalil, K. S.; Varanasi, K. K. Drag reduction using lubricant-impregnated surfaces in viscous laminar flow. *Langmuir* **2014**, *30*, 10970–10976.

(25) Kim, J. H.; Rothstein, J. P. Delayed lubricant depletion on liquid-infused randomly rough surfaces. *Exp. Fluids* **2016**, *57*, 9.

(26) Rosenberg, B. J.; Van Buren, T.; Fu, M. K.; Smits, A. J. Turbulent drag reduction over air- and liquid- impregnated surfaces. *Phys. Fluids* **2016**, *28*, 015103.

(27) Wang, Y.; Zhang, H. F.; Liu, X. W.; Zhou, Z. P. Slippery liquid-infused substrates: a

versatile preparation, unique anti-wetting and drag-reduction effect on water. *J. Mater. Chem. A* **2016**, *4*, 2524–2529.

(28) Fu, M. K.; Arenas, I.; Leonardi, S.; Hultmark, M. Liquid-infused surfaces as a passive method of turbulent drag reduction. *J. Fluid Mech.* **2017**, *824*, 688–700.

(29) Asmolov, E. S.; Nizkaya, T. V.; Vinogradova, O. I. Enhanced slip properties of lubricant-infused grooves. *Phys. Rev. E* **2018**, *98*, 033103.

(30) García-Cartagena, E. J.; Arenas, I.; An, J.; Leonardi, S. Dependence of the drag over superhydrophobic and liquid infused surfaces on the asperities of the substrate. *Phys. Rev. Fluids* **2019**, *4*, 114604.

(31) Lee, S. J.; Kim, H. N.; Choi, W.; Yoon, G. Y.; Seo, E. A nature-inspired lubricant-infused surface for sustainable drag reduction. *Soft Matter* **2019**, *15*, 8459–8467.

(32) Vega-Sánchez, C.; Peppou-Chapman, S.; Zhu, L.; Neto, C. Nanobubbles explain the large slip observed on lubricant-infused surfaces. *Nature Communications* **2022**, *13*, 351.

(33) Peppou-Chapman, S.; Neto, C. Depletion of the Lubricant from Lubricant-Infused Surfaces due to an Air/Water Interface. *Langmuir* **2021**, *37*, 3025–3037.

(34) Peppou-Chapman, S.; Neto, C. Mapping Depletion of Lubricant Films on Antibiofouling Wrinkled Slippery Surfaces. *ACS Appl. Mater. Interf.* **2018**, *10*, 33669–33677.

(35) Schoenecker, C.; Baier, T.; Hardt, S. Influence of the enclosed fluid on the flow over a microstructured surface in the Cassie state. *J. Fluid Mech.* **2014**, *740*, 168–195.

(36) Alinovi, E.; Bottaro, A. Apparent slip and drag reduction for the flow over superhydrophobic and lubricant-impregnated surfaces. *Phys. Rev. Fluids* **2018**, *3*, 1–22.

(37) Ge, Z.; Holmgren, H.; Kronbichler, M.; Brandt, L.; Kreiss, G. Effective slip over partially filled microcavities and its possible failure. *Phys. Rev. Fluids* **2018**, *3*, 1–17.

(38) Vega-Sánchez, C.; Neto, C. Pressure Drop Measurements in Microfluidic Devices: A Review on the Accurate Quantification of Interfacial Slip. *Adv. Mater. Interfaces* **2022**, *9*, 2101641.

(39) Vinogradova, O. Slippage of water over hydrophobic surfaces. *Int. J. Miner. Process.* **1999**, *56*, 31–60.

(40) Butt, H. J.; Cappella, B.; Kappl, M. Force measurements with the atomic force microscope: Technique, interpretation and applications. *Surface Science Reports* **2005**, *59*, 1–152.

(41) Anaconda Software Distribution. 2020; `https://docs.anaconda.com/`.

(42) Peppou-Chapman, S.; Neto, C. AFM Nanobubble Mapping. 2021; `https://github.com/speppou/AFM_Nanobubble_Mapping`.

(43) Friedrich, S.; Cappella, B. Study of Micro- and Nanoscale Wetting Properties of Lubricants Using AFM Force–Distance Curves. *Tribol. Lett.* **2020**, *68*, 36.

(44) Mate, C. M.; Lorenz, M. R.; Novotny, V. J. Determination of Lubricant Film Thickness on a Particulate Disk Surface by Atomic Force Microscopy. *IEEE Trans. Magn.* **1990**, *26*, 1225–1228.

(45) Mate, C. M.; Lorenz, M. R.; Novotny, V. J. Atomic force microscopy of polymeric liquid films. *J. Chem. Phys.* **1989**, *90*, 7550–7555.

(46) Ally, J.; Vittorias, E.; Amirfazli, A.; Kappl, M.; Bonaccurso, E.; McNamee, C. E.; Butt, H.-J. Interaction of a Microsphere with a Solid-Supported Liquid Film. *Langmuir* **2010**, *26*, 11797–11803.

(47) Scarratt, L. R. J.; Zhu, L.; Neto, C. How Slippery are SLIPS? Measuring Effective Slip on Lubricated Surfaces with Colloidal Probe Atomic Force Microscopy. *Langmuir* **2019**, *35*, 2976–2982.

(48) An, H.; Tan, B. H.; Ohl, C.-D. Distinguishing Nanobubbles from Nanodroplets with AFM: The Influence of Vertical and Lateral Imaging Forces. *Langmuir* **2016**, *32*, 12710–12715.

(49) Tyrrell, J. W.; Attard, P. Images of nanobubbles on hydrophobic surfaces and their interactions. *Phys. Rev. Lett.* **2001**, *87*, 1–4.

(50) Walczyk, W.; Schönherr, H. Dimensions and the Profile of Surface Nanobubbles: Tip-Nanobubble Interactions and Nanobubble Deformation in Atomic Force Microscopy. *Langmuir* **2014**, *30*, 11955–11965.

(51) Walczyk, W.; Schönherr, H. Characterization of the interaction between AFM tips and surface nanobubbles. *Langmuir* **2014**, *30*, 7112–7126.

(52) Wang, X.; Zhao, B.; Hu, J.; Wang, S.; Tai, R.; Gao, X.; Zhang, L. Interfacial gas nanobubbles or oil nanodroplets? *Phys. Chem. Chem. Phys.* **2017**, *19*, 1108–1114.

(53) Tonelli, M.; Peppou-Chapman, S.; Ridi, F.; Neto, C. Effect of Pore Size, Lubricant Viscosity, and Distribution on the Slippery Properties of Infused Cement Surfaces. *J. Phys. Chem. C* **2019**, *123*, 2987–2995.

(54) Zhao, B.; Song, Y.; Wang, S.; Dai, B.; Zhang, L.; Dong, Y.; Lü, J.; Hu, J. Mechanical mapping of nanobubbles by PeakForce atomic force microscopy. *Soft Matter* **2013**, *9*, 8837.

(55) Cappella, B. Force-distance curves on lubricant films: An approach to the characterization of the shape of the AFM tip. *Micron* **2017**, *93*, 20–28.

(56) Kreder, M. J.; Daniel, D.; Tetreault, A.; Cao, Z. L.; Lemaire, B.; Timonen, J. V. I.; Aizenberg, J. Film Dynamics and Lubricant Depletion by Droplets Moving on Lubricated Surfaces. *Phys. Rev. X* **2018**, *8*, 31053.

(57) Attard, P. Direct Measurement of the Surface Tension of Nanobubbles. *arXiv (Cond. Soft Matter)* **2015**, *https://doi.org/10.48550/arXiv.1505.02217*.

(58) An, H.; Liu, G.; Atkin, R.; Craig, V. S. Surface Nanobubbles in Nonaqueous Media: Looking for Nanobubbles in DMSO, Formamide, Propylene Carbonate, Ethylammonium Nitrate, and Propylammonium Nitrate. *ACS Nano* **2015**, *9*, 7596–7607.

(59) Dupré De Baubigny, J.; Benzaquen, M.; Fabié, L.; Delmas, M.; Aimé, J. P.; Legros, M.; Ondarçuhu, T. Shape and Effective Spring Constant of Liquid Interfaces Probed at the Nanometer Scale: Finite Size Effects. *Langmuir* **2015**, *31*, 9790–9798.

TOC Graphic

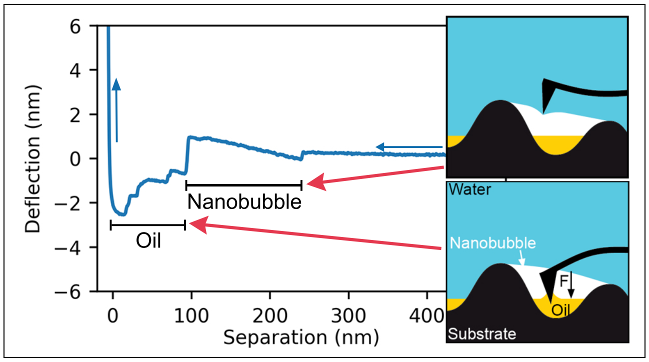
6
4
2
0
−2
−4
−6
Deflection (nm)
0
100
200
300
400
Separation (nm)
Nanobubble
Oil
Water
Nanobubble
F
Oil
Substrate